CHEMISTRY OF MATERIALS
ARTICLE
pubs.acs.org/cm

Fe_3Se_4 Nanostructures with Giant Coercivity Synthesized by Solution Chemistry

Hongwang Zhang,[†] Gen Long,[†] Da Li,[†,‡] Renat Sabirianov,[§] and Hao Zeng[*,†]

[†]Department of Physics, University at Buffalo, the State University of New York, Buffalo, New York 14260, United States
[‡]Shenyang National Laboratory for Materials Science, Institute of Metal Research and International Center for Materials Physics, Chinese Academy of Sciences, Shenyang, Liaoning 110016, China
[§]University of Nebraska—Omaha, Omaha, Nebraska 68182, United States

Supporting Information

ABSTRACT: Fe_3Se_4 nanostructures have been synthesized by a one-pot high-temperature organic-solution-phase method. The size of these nanostructures can be tuned from 50 to 500 nm, and their shapes can be varied from nanosheets and nanocacti to nanoplatelets. These nanostructures exhibit hard magnetic properties, with giant coercivity values reaching 40 kOe at 10 K and 4 kOe at room temperature. The estimated magnetocrystalline anisotropy constant is 6×10^6 erg cm^{-3}, comparable to that of hexagonal close-packed cobalt. The magnetic properties can be further tuned by substituting Fe ions by other transition-metal elements such as Co.

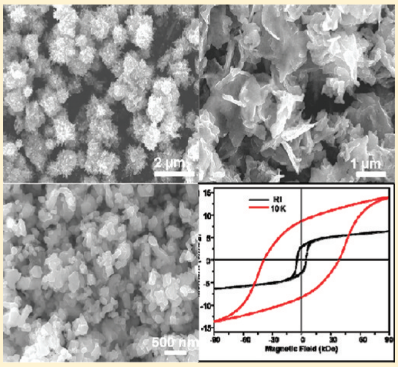

KEYWORDS: Fe_3Se_4, ferrimagnetic, magnetic nanostructures, hard magnetic materials

Hard magnetic materials with large coercivity have broad applications ranging from high-density data storage media to permanent magnets.[1−8] Most hard magnetic materials contain a noble metal (such as FePt)[7,8] or rare-earth element (e.g., $SmCo_5$, Sm_2Co_{17}, and $Nd_2Fe_{14}B$).[9−14] The strong influence from the crystal field with low symmetry and spin−orbit coupling gives rise to large magnetocrystalline anisotropy, which is the origin of the hard magnetic properties. Typically large anisotropy of a material can only be achieved after high-temperature annealing to bring out the chemically ordered phase of an intermetallic compound. The high cost and scarcity of noble-metal and rare-earth elements motivated people to search for hard magnetic materials without these elements. However, it is rare for compounds without noble-metal or rare-earth elements to exhibit large anisotropy and coercivity.

Iron chalcogenide compounds have been studied dating back to the 1950s and 1960s.[15−19] Two well-known magnetic compounds are a hexagonal phase with the approximate composition of Fe_7Se_8 (H-phase) and a monoclinic phase with an approximate composition of Fe_3Se_4 (M-phase). In both of them, Fe and Se ions occupy alternating layers along the *c*-axis. Both compounds are ferrimagnetic with Curie temperatures of 450 K for Fe_7Se_8 and 314 K for Fe_3Se_4.[15−19] The ferrimagnetism is associated with the ordered iron vacancies similar to pyrrhotite Fe_7S_8.[20,21] In a Fe_3Se_4 unit cell, the vacancies of Fe appear in every other Fe layer, and the number of vacancies alternates between different layers. The lattice vacancies are aligned along the *b*-axis and adopt a body-centered structure in a unit cell. All these vacancies lie in the $(\bar{1}01)$ plane as shown in Figure 1. The ferrimagnetism thus originates from such an ordered arrangement of Fe vacancies.[16] Recently, iron chalcogenide compounds have received renewed interest due to the discovery of superconductivity in the tetragonal PbO-type $FeSe_{1-x}$.[22] Iron chalcogenides have the simplest crystal structure among all Fe-based superconductors and are nontoxic. They are therefore an important family of materials for the investigation of the superconducting mechanism.

While Fe-based magnetic nanostructures including iron and or other transition metals,[23−30] iron oxides[31−36] and alloys,[37−40] and chalcogenide semiconductor nanostructures[41,42] have all been extensively studied, the magnetic properties of iron chalcogenide nanostructures and other chalcogenide-based compounds have received attention only very recently.[43−46] The reduced dimensionality may provide additional tuning capabilities for magnetism and other physical properties. There are only a couple of recent publications reporting the synthesis of FeSe sheets by chemical solution methods.[47,48] No superconductivity has been found, possibly due to small dimensions or off-stoichiometry.[47] A very recent work reported the synthesis and magnetic properties of Fe_7Se_8 and Fe_3Se_4 nanostructures.[49] However, the magnetic anisotropy in these materials, whether in bulk form or in nanostructures, especially for Fe_3Se_4, is less studied. Here, we report a facile one-pot synthesis of Fe_3Se_4 magnetic nanostructures by utilizing the organic-solution-phase chemical

Received: June 8, 2011
Revised: June 19, 2011
Published: July 21, 2011

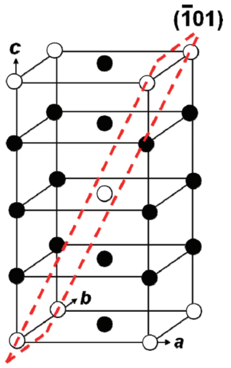

Figure 1. Schematic of the unit cell of Fe_3Se_4. Open and solid circles represent vacancies and Fe atoms. Se atoms are omitted for clarity. Reprinted with permission from ref 16. Copyright 1956 the Physical Society of Japan.

decomposition method. The as-synthesized Fe_3Se_4 nanostructures exhibit coercivity values of up to 40 kOe at 10 K, with a room-temperature value of 4.0 kOe. The low-temperature anisotropy constant is thus estimated to be greater than 6×10^6 erg cm^{-3}. To our knowledge, such a large coercivity has not been reported previously in Fe_3Se_4 or in any other as-synthesized magnetic systems.

EXPERIMENTAL SECTION

Materials. Iron(III) 2,4-pentanedionate [$Fe(acac)_3$], iron(II) chloride tetrahydrate ($FeCl_2.4H_2O$; 99%), cobalt(II) 2,4-pentanedionate [$Co(acac)_2$], oleic acid (90%), and Se (powder, 99.999%) were purchased from Alfa Aesar. Oleylamine (80−90%) was obtained from Acros Organics. All chemicals were used without further purification.

Synthesis of Fe_3Se_4 Nanocacti. In a typical reaction, 0.53 g (1.5 mmol) of $Fe(acac)_3$ and 0.158 g (2 mmol) of Se powders were mixed in 15 mL of oleylamine in a 125 mL four-neck flask. Under a nitrogen flow, the mixture was first heated to 120 °C. The solution was kept at this temperature for 60 min to remove low boiling point solvents and oxygen. Then the temperature was raised to 200 °C at a ramping rate of 2 °C min^{-1} and kept at 200 °C for 60 min. At a ramping rate of 5 °C min^{-1} the solution was brought to 300 °C and kept at 300 °C for 60 min. The solution was cooled to room temperature by removing the heating source. The Fe_3Se_4 nanoparticles were precipitated by adding 20 mL of 2-propanol and centrifuged at 5000 rpm for 5 min. The precipitates were rewashed by 15 mL of hexane and 10 mL of 2-propanol.

Synthesis of Fe_3Se_4 Nanosheets. This synthesis is similar to the synthesis of Fe_3Se_4 spherical particles except that 8 mL of oleic acid was added to the mixture before the reaction.

Synthesis of Fe_3Se_4 Faceted Nanoplatelets. A 0.16 g (0.8 mmol) portion of $FeCl_2.4H_2O$ and 0.079 g (1 mmol) of Se powders were mixed in 15 mL of oleylamine and 1 mL of oleic acid in a 125 mL four-neck flask. The mixture was heated to 120 °C and kept at 120 °C for 60 min and the heated to and kept at 300 °C for another 60 min.

Synthesis of $Co_xFe_{2-x}Se_4$ Nanoparticles. $Fe(acac)_3$ and $Co(acac)_2$ in a certain ratio (total 1.5 mmol) and 0.158 g (2 mmol) of Se powders were mixed in 15 mL of oleylamine in a 125 mL four-neck flask. The mixture was heated to 120 °C and kept at 120 °C for 60 min and then heated to and kept at 300 °C for another 60 min.

Structural Characterizations. The size and morphology of the nanostructures as well as the high-resolution lattice images were characterized by using a JEOL 2010 (200 kV) transmission electron microscope. The compositions were characterized by Oxford energy-dispersive X-ray spectroscopy (EDS). The scanning electron microscopy (SEM) images and elemental mapping were obtained with a Carl Zeiss Auriga CrossBeam focused ion beam/field-emission SEM (FIB/SEM) system. Powder X-ray diffraction (XRD) patterns of the nanoparticles were recorded on a Bragg−Brentano geometry using a Rigaku Ultima IV instrument with Cu Kα radiation (λ = 1.5418 Å). Magnetic measurements were performed using the vibrating sample magnetometer option of a Quantum Design physical property measurement system (PPMS), model 6000, with a field of up to 90 kOe.

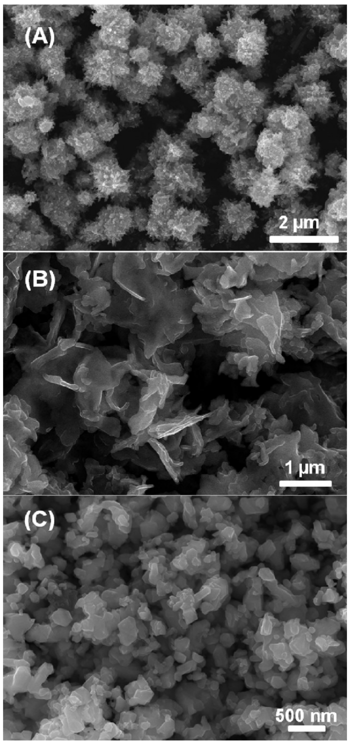

Figure 2. Typical SEM images of as-synthesized Fe_3Se_4 (A) nanocacti, (B) nanosheets, and (C) nanoplatelets.

RESULTS AND DISCUSSION

Structural Properties. We applied a simple one-pot solution-phase method to synthesize the Fe_3Se_4 nanostructures by heating a mixture of iron salts in a coordinating organic solvent. In a solvothermal synthesis, there are a number of external knobs that can be tuned to control the morphology of the as-synthesized nanostructures. The most effective ones are the reaction temperature, time, strength of the coordination ligands and/or solvents, and polarity of the solvents. For example, in our earlier work, we demonstrated that the polarity of the solvent can be used to control the shape of hybrid nanostructures in seed-mediated growth.[50,51] In the present work, the material we are synthesizing is special in that Fe_3Se_4 is a naturally layered material with weak bonding along the $(\bar{1}01)$ planes. At the beginning stage of the reaction, sheetlike or plateletlike nanostructures tend to form. This is confirmed by our extensive SEM and transmission electron microscopy (TEM) investigations. By controlling the nucleation rate, and using different coordination ligands to control the growth rate in the lateral or vertical directions, we can obtain a wealth of morphologies. To demonstrate this general design principle, we show a few examples below.

Using $Fe(acac)_3$ and oleylamine as both the solvent and surfactant, we can obtain nanoparticles with an interesting morphology shown in the SEM image (Figure 2A). These nanoparticles are generally of spherical shape, with numerous spikes grown on the

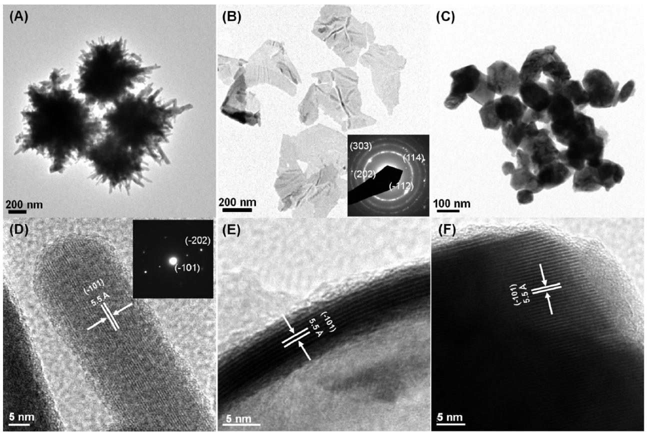

Figure 3. Typical TEM images of (A) the as-synthesized Fe_3Se_4 nanocacti with rodlike features growing on the surface, (B) several isolated Fe_3Se_4 nanosheets, and (C) the as-synthesized Fe_3Se_4 nanoplatelets. HRTEM images of (D) the rodlike features growing on the surface of Fe_3Se_4 nanocacti, (E) the edge of a rolled-up Fe_3Se_4 nanosheet revealing its thickness; and (F) the as-synthesized Fe_3Se_4 nanoplatelets. The lattice fringe space at 5.5 Å represents the $(\bar{1}01)$ planes (5.51 Å) of Fe_3Se_4.

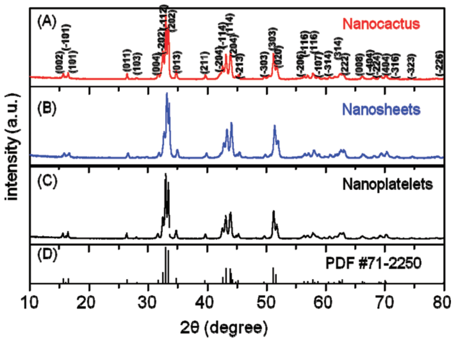

Figure 4. XRD patterns of (A) the as-synthesized Fe_3Se_4 nanocacti (red curve), (B) the Fe_3Se_4 nanosheets (blue curve), and (C) the faceted Fe_3Se_4 nanoplatelets (black curve) and (D) the standard XRD pattern of monoclinic Fe_3Se_4 (JCPDS card no. 71-2250).

surface pointing radically outward, resembling a cactus plant. The detailed morphology of the Fe_3Se_4 nanocacti is shown in the TEM image (Figure 3A), with rodlike features growing perpendicularly to their surfaces (Figure S1, Supporting Information). The average size of the nanocacti is about 500 nm. XRD patterns were used to characterize the crystal structure of the Fe_3Se_4 nanocacti. As shown in Figure 4A, the XRD peaks of the as-synthesized Fe_3Se_4 nanocacti match well with the standard XRD pattern of bulk Fe_3Se_4 (JCPDS card no. 71-2250) that has a monoclinic structure with a space group of $I2/m(12)$ and a = 6.208 Å, b = 3.541 Å, and c = 11.281 Å (Figure 4D). The Fe_3Se_4 grain size is about 32 nm, as estimated from the width of the (211) diffraction peak of the XRD pattern using Scherrer's formula. Elemental mapping and the compositional line profile of a single nanocactus reveal the even distribution of Fe and Se in the particle (Figure 5). This suggests that, to the detection limit of the instrument, the particle is in a single phase. The relative molar ratio of Fe to Se in the nanocactus was examined by EDS elemental analyses (Figure S2, Supporting Information). From the EDS spectrum, only Fe and Se peaks were observed, and the Fe/Se average atomic ratio is 44.3/55.7 (1/1.26), close to the stoichiometric ratio of Fe_3Se_4. Close examination of the rodlike features on the surface by high-resolution TEM (HRTEM) suggests that they are single-crystalline nanorods (Figure 3D). The HRTEM image of a nanorod shows lattice fringes parallel to the long axis, with a lattice fringe spacing at approximately 5.5 Å, which represents the $(\bar{1}01)$ planes (5.51 Å) of the monoclinic Fe_3Se_4. The selected area electron diffraction (SAED) pattern of the single-crystalline nanorods (Figure 3D, inset) further demonstrates that the long axis of the rod is parallel to the $(\bar{1}01)$ planes.

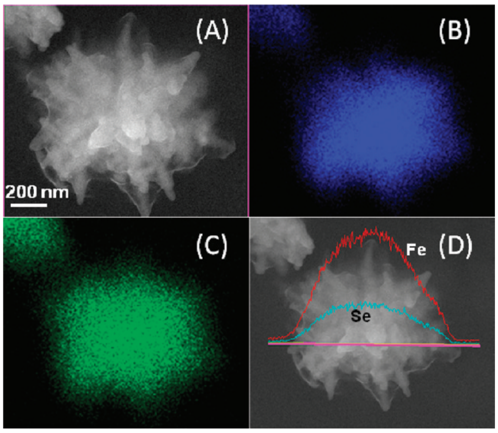

Figure 5. (A) SEM image of a single nanocactus, elemental mapping of (B) Se and (C) Fe, and (D) line-scan EDS analysis across the nanoparticle measured by a Carl Zeiss FIB/SEM system.

The growth mechanism can be explained as follows: At the beginning stage of the reaction, sheetlike structures are formed due to the ordered Fe vacancies in the $(\bar{1}01)$ planes. $Fe(acac)_3$ is a ferric coordination complex which is rather stable and only starts to decompose in the solvent upon heating to 200 °C. By remaining at that temperature, the growth rate is slow. Oleylamine, a weak coordination solvent, is chosen as both a solvent and surfactant. Thus, it allows sufficient lateral growth to form larger sheets only a few atomic layers thick. Upon heating to higher temperatures (300 °C), the layered structures eventually cluster and sinter to form solid nanospheres, with nanorods residing on their surfaces. These nanorods do not grow along the axial direction as most growth mechanisms of nanorods would suggest, but rather originate from sintered nanosheets, and the $(\bar{1}01)$ planes are thus parallel to the long axis.

Keeping everything else the same, but adding a stronger coordination surfactant such as oleic acid during the reaction, the growth along the lateral directions is also suppressed. This would lead to smaller nanosheets with lateral dimensions of only a few hundred nanometers. These smaller nanosheets appear to be strong enough to form either stand-alone structures or form clusters. The SEM image in Figure 2B shows that most of these nanosheets grow into clusters, producing flowerlike patterns. Figure 3B shows the TEM image of several isolated nanosheets. Most of these isolated nanosheets lie conformally to the surface of the TEM grid. However, a few have their edges rolled up to be parallel to the grid, allowing the identification of the atomic planes forming the nanosheets and their thicknesses. From the HRTEM image (Figure 3E), the thickness of the nanosheets can be clearly observed to range between 2 and 4 nm, corresponding to 2−4 unit cells of the monoclinic Fe_3Se_4. The atomic plane forming the sheets is identified to be the $(\bar{1}01)$ plane from the lattice spacing of 5.50 Å. The SAED pattern (inset in Figure 3B) suggests that the isolated nanosheets are polycrystalline. The three diffraction rings can be identified as $(\bar{1}12)/(202)$, $(\bar{1}14)/(114)$, and $(303)/(020)$. The absence of the diffraction from the $(\bar{1}01)$ planes is consistent with the fact that the $(\bar{1}01)$ planes are parallel to the sheets. The XRD pattern (Figure 4B) of the nanosheets can be indexed to monoclinic Fe_3Se_4 as well. The EDS analysis confirmed that the Fe/Se atomic ratio was 43.3/56.7 (1/1.31), which is very close to the stoichiometric ratio of 3/4.

To accelerate the initial nucleation rate, the coordination complex $Fe(acac)_3$ can be replaced by an inorganic metal salt such as $FeCl_2.4H_2O$. The faster nucleation leads to much smaller particles with sizes of only about 100 nm. In the presence of oleic acid, highly faceted Fe_3Se_4 nanoplatelets were generated, as shown in the SEM image of Figure 2C and TEM image of Figure 3C. The HRTEM image (Figure 3F) shows the lattice spacing of 5.5 Å, corresponding to the $(\bar{1}01)$ plane of Fe_3Se_4. The grain size of the nanoparticles is estimated to be about 45 nm from the (211) diffraction peak of the XRD pattern (Figure 4C).

It should be emphasized that the initially formed iron selenide compound is iron deficient, and the stoichiometry of 3/4 can only be achieved after prolonged reaction. To confirm this, a small portion of the reaction mixture was withdrawn from the reaction flask at 200 °C and quenched by injection into a 2-propanol/hexane solution. The crystalline structure of collected particles was studied by XRD (Figure S3, Supporting Information). The major diffraction peaks of the particles (Figure S3B) are indexed to orthorhombic $FeSe_2$ (JCPDS card no. 79-1892, Figure S3A) with a space group of *Pnnm* (No. 58). Very weak Fe_3Se_4 peaks can also be observed. Similarly, the particles obtained at a reaction temperature of 250 °C shows both $FeSe_2$ and Fe_3Se_4 phases with comparable diffraction peak intensities (Figure S3C). This indicates that a change from $FeSe_2$ to Fe_3Se_4 occurred during the reaction. Pure Fe_3Se_4 phase was obtained at 300 °C. From the above results, we can conclude that although Fe_3Se_4 is the thermodynamically stable phase, Fe diffusion into Se is a slow process at our reaction temperature. In our reactions, both oleylamine and oleic acid served as solvents as well as surfactants to form iron complexes with iron precursors. The decomposition of iron complexes at elevated temperatures is accompanied by nucleation/growth processes. It is known that Fe_3Se_4 crystallizes in a monoclinic structure with ordered Fe vacancies on every second metal layer. It is therefore expected that Fe_3Se_4 tends to cleave along the $(\bar{1}01)$ plane to form layered nanostructures.[16]

Our synthesis method is simple without the need for hot injection as described in previous syntheses, in which a large amount of excess Se is needed to compensate for the evaporation of Se during the dissolution process.[44,46] In our approach, by premixing the precursors in stoichiometric ratio and heating to above 200 °C for a prolonged period, Fe ions are allowed to slowly diffuse into the Se to complete the formation of pure Fe_3Se_4 without phase separation. The phase purity is confirmed by structural and magnetic measurements. FeSe, Fe_7Se_8, and $FeSe_2$ compound nanoparticles can also be produced by this method by changing the precursor ratio and reaction conditions. Under our synthetic conditions, hot injection of either Se in trioctylphosphine or $Fe(acac)_3$ in oleylamine into the reaction solution containing other precursors, as has been done in earlier work, led to phase separation, and no Fe_3Se_4 phase was formed.

Magnetic Properties. All of the Fe_3Se_4 nanocacti, nanosheets, and nanoplatelets exhibit hard magnetic properties, and their magnetic hysteresis loops are shown in Figure 6. The coercivity of nanocacti reaches 3.4 kOe at room temperature, which rises more than 10-fold to about 36 kOe at 10 K (Figure 6A). There seems to be a paramagnetic component, since the hysteresis loops do not reach saturation even at a field of 90 kOe. This suggests that either the anisotropy field is much larger than 90 kOe or the spins in the system are noncollinear. It is not clear at this stage whether this spin canting occurs at the grain boundaries or within the whole nanostructure. The magnetization at 90 kOe is ~5 emu g^{-1} at 300 K, which increases to ~15 emu g^{-1} at 10 K. These results represent lower bounds of

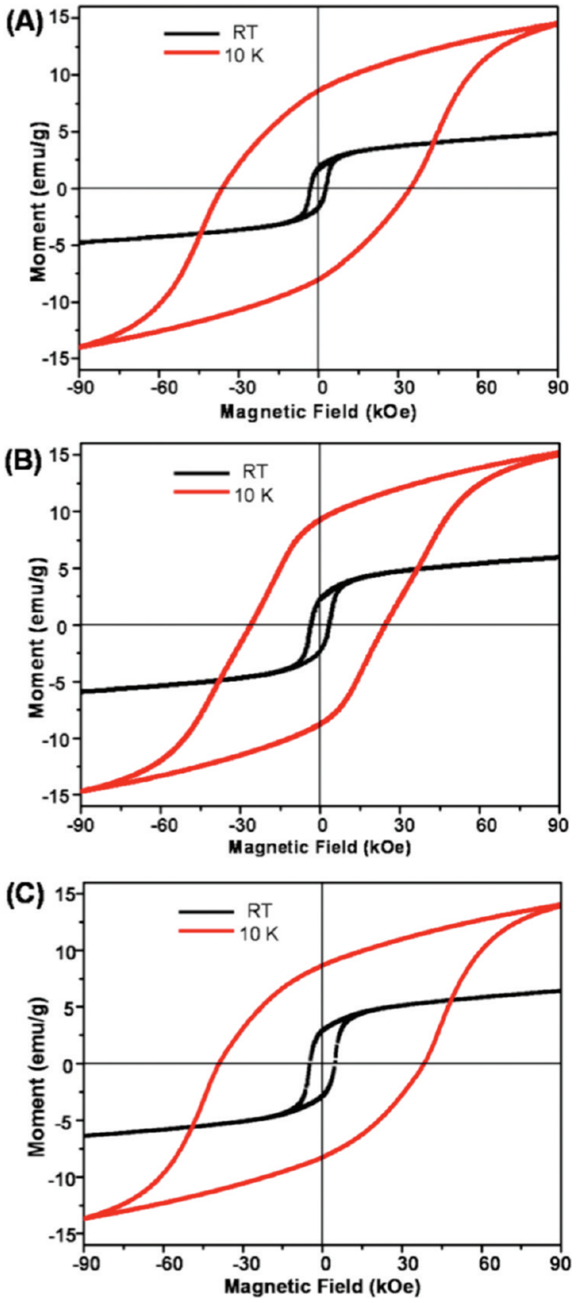

Figure 6. Hysteresis loops of (A) Fe_3Se_4 nanocacti, (B) Fe_3Se_4 nanosheets, and (C) faceted Fe_3Se_4 nanoparticles measured by the vibrating sample magnetometer option of a PPMS with a field of 90 kOe at 10 K (red curves) and at room temperature (black curves). The 10 K hysteresis loops were measured after zero-field cooling.

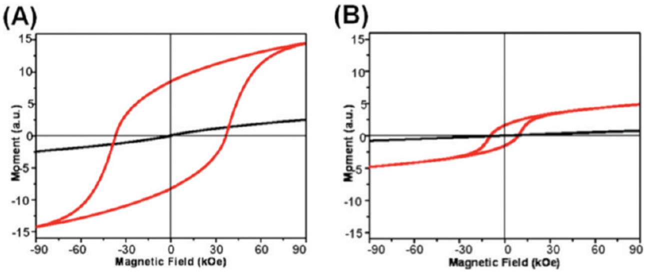

Figure 7. Hysteresis loops of (A) $Co_{0.2}Fe_{2.8}Se_4$ nanoparticles and (B) $CoFe_2Se_4$ nanoparticles measured by the vibrating sample magnetometer option of a PPMS with a field of 90 kOe at 10 K (red curves) and room temperature (black curves). The 10 K hysteresis loops were measured after zero-field cooling.

Table 1. Magnetic Parameters Measured for Fe_3Se_4 Nanoplatelets and $Co_xFe_{2-x}Se_4$ Nanoparticles

phase	coercivity at room temp (kOe)	coercivity at 10 K (kOe)	saturation magnetization at 10 K (emu/g)	Curie temp (K)
Fe_3Se_4	4	40	~15	320
$Co_{0.2}Fe_{2.8}Se_4$	0	37	~15	290
$CoFe_2Se_4$	0	9	5	<200

the saturation magnetization values. The strong temperature dependence of the magnetization and coercivity suggests that the Curie temperature is close to room temperature, which is supported by our thermal magnetization measurements (Figure S4, Supporting Information). Our result is also consistent with earlier reports of $T_c \approx 320$ K for Fe_3Se_4.[15−19] Using the measured magnetization and coercivity values, the lower bounds of the magnetic anisotropy constant can be estimated to be 2×10^5 erg cm^{-3} at 300 K and 6×10^6 erg cm^{-3} at 10 K. Since Fe_3Se_4 has low magnetization, shape anisotropy does not play a significant role, and the magnetocrystalline anisotropy dominates the total anisotropy. The anisotropy constant at 10 K is comparable to that of bulk cobalt and is an order of magnitude higher than that of Fe_3O_4 at 2×10^5 erg cm^{-3}. This difference most likely originates from the monoclinic structure of Fe_3Se_4, which has a crystal field with a lower symmetry than that of cubic spinel structured Fe_3O_4. The detailed mechanism of the large anisotropy is investigated by first-principles computation. Our calculation shows that the easy axis is *b*, in agreement with the experimental findings. The results show that the magnetocrystalline anisotropy energy is 2.05 meV/unit cell, which corresponds to 1.2×10^7 erg cm^{-3}. Both Fe_3Se_4 nanosheets and faceted nanoparticles show similar magnetic hysteresis loops. The nanosheets have a lower coercivity of 29 kOe at 10 K (Figure 6B), while the nanoplatelets show higher coercivity values of 40 kOe at 10 K and 4.0 kOe at room temperature (Figure 6C). The different coercivity values may originate from the difference in grain sizes and stoichiometry. Other interesting physical properties originating from the strong 2D confinement of the nanosheets are currently under investigation.

It is interesting to note the similarity and differences between Fe_3Se_4 and the more extensively investigated spinel magnetite Fe_3O_4. They are both ferrimagnetic materials with similar chemical formulas. However, their magnetocrystalline anisotropies differ by more than an order of magnitude, perhaps due mainly to different crystal symmetries. On the other hand, the Fe ions in magnetite can be easily substituted by other transition metals to form different spinel ferrites with varying magnetic properties. For example, $CoFe_2O_4$ is a hard ferrite with a magnetocrystalline anisotropy of 2×10^6 erg cm^{-3}.[32] This substitution of Fe with other transition-metal ions should also be possible with Fe_3Se_4. As an example of such substitution, we investigated Co-doped Fe_3Se_4 nanostructures $Co_xFe_{3-x}Se_4$, with x ranging from 0 to 1. Co was incorporated into the Fe_3Se_4 nanostructures by adding $Co(acac)_2$ to the precursor solution. The sizes of $Co_xFe_{3-x}Se_4$ nanoparticles tend to be reduced by increasing the Co amount. $Co_{0.2}Fe_{2.8}Se_4$ nanoparticles have an average size of ~100 nm, while the sizes of $CoFe_2Se_4$ nanoparticles are around 50 nm (Figure S5A,B, Supporting Information). The XRD pattern showed that the monoclinic structure is retained. The saturation magnetization initially stays constant and then decreases significantly when x increases to 1. The coercivity and Curie temperature both decrease with increasing Co concentration. The coercivity of the nanoparticles at 10 K is reduced to 37 kOe for $x = 0.2$ and further decreases to 9 kOe for $x = 1$ (Figure 7). The Curie temperature is 290 K for $x = 0.2$ and is reduced to less than 200 K for $x = 1$. As a result, the hysteresis loops at room temperature show paramagnetic behavior for Co-doped samples. The magnetic properties of Fe_3Se_4 nanoplatelets and $Co_xFe_{3-x}Se_4$ nanoparticles are summarized in Table 1. This example shows that the magnetic properties of Fe_3Se_4 can be significantly modified by doping with other transition-metal elements.

CONCLUSIONS

In conclusion, we have developed a facile protocol for synthesizing Fe_3Se_4 nanostructures by the high-temperature organic-solution-phase method. Giant coercivity values as high as 40 kOe at 10 K and 4.0 kOe at room temperature can be achieved for the as-synthesized nanostructures. Despite the large coercivity, the energy product is low due to the low saturation magnetization of the material and low Curie temperature. However, as has been demonstrated, the magnetic property is easily tunable by doping. Coordinated theoretical and experimental work is under way to investigate whether the saturation magnetization, magnetocrystalline anisotropy, and Curie temperature can be enhanced by doping. If these properties are enhanced, Fe_3Se_4-based materials can be a low-cost, nontoxic alternative to noble-metal- or rare-earth-element-based advanced magnets.

ASSOCIATED CONTENT

Ⓢ **Supporting Information.** Additional characterization data (PDF). This material is available free of charge via the Internet at http://pubs.acs.org.

AUTHOR INFORMATION

Corresponding Author

*E-mail: haozeng@buffalo.edu.

ACKNOWLEDGMENT

We thank Peter Bush and Yueling Qin for SEM and HRTEM measurements. This work was supported by National Science Foundation Grant DMR0547036.

■ REFERENCES

(1) Cullity, B. D. *Introduction to Magnetic Materials*; Addison-Wesley Publishing Co.: Reading, MA, 1972.

(2) Aharoni, A. *Introduction to the Theory of Ferromagnetism*; Oxford University Press: New York, 1996.

(3) Skomski, R.; Coey, J. M. D. *Permanent Magnetism*; Institute of Physics Publishing: Bristol, U.K., Philadelphia, PA, 1999.

(4) Weller, D.; Doerner, M. F. *Annu. Rev. Mater. Sci.* **2000**, *30*, 611–644.

(5) Sun, S. H. *Adv. Mater.* **2006**, *18*, 393–403.

(6) Zhang, H. W.; Liu, Y.; Sun, S. H. *Front. Phys. China* **2010**, *5*, 347–356.

(7) Sun, S. H.; Murray, C. B.; Weller, D.; Folks, L.; Moser, A. *Science* **2000**, *287*, 1989–1992.

(8) Zeng, H.; Li, J.; Liu, J. P.; Wang, Z. L.; Sun, S. H. *Nature* **2002**, *420*, 395–398.

(9) Fullerton, E. E.; Jiang, J. S.; Bader, S. D. *J. Magn. Magn. Mater.* **1999**, *200*, 392–404.

(10) Hasegawa, M.; Uchida, K.; Nozawa, Y.; Endoh, M.; Tanigawa, S.; Sankar, S. G.; Tokunaga, M. *J. Magn. Magn. Mater.* **1993**, *124*, 325–329.

(11) Gu, H. W.; Xu, B.; Rao, J. C.; Zheng, R. K.; Zhang, X. X.; Fung, K. K.; Wong, C. Y. C. *J. Appl. Phys.* **2003**, *93*, 7589–7591.

(12) Hou, Y. L.; Xu, Z. C.; Peng, S.; Rong, C. B.; Liu, J. P.; Sun, S. H. *Adv. Mater.* **2007**, *19*, 3349–3352.

(13) Liu, J. P. *JOM* **2010**, *62*, 56–61.

(14) Zhang, H. W.; Peng, S.; Rong, C. B.; Liu, P.; Zhang, Y.; Kramer, M. J.; Sun, S. H. *J. Mater. Chem.* **2011**, Advance Article, DOI: 10.1039/C1JM11753J.

(15) Hirone, T.; Chiba, S. *J. Phys. Soc. Jpn.* **1956**, *11*, 666–670.

(16) Okazaki, A.; Hirakawa, K. *J. Phys. Soc. Jpn.* **1956**, *11*, 930–936.

(17) Hirakawa, K. *J. Phys. Soc. Jpn.* **1957**, *12*, 929–938.

(18) Kamimura, T.; Kamigaki, K.; Hirone, T.; Sato, K. *J. Phys. Soc. Jpn.* **1967**, *22*, 1235–1240.

(19) Terzieff, P.; Komarek, K. L. *Monatsh. Chem.* **1978**, *109*, 1037–1047.

(20) Okazaki, A. *J. Phys. Soc. Jpn.* **1961**, *16*, 1162–1170.

(21) Takemura, Y.; Suto, H.; Honda, N.; Kakuno, K.; Saito, K. *J. Appl. Phys.* **1997**, *81*, 5177–5179.

(22) Hsu, F. C.; Luo, J. Y.; Yeh, K. W.; Chen, T. K.; Huang, T. W.; Wu, P. M.; Lee, Y. C.; Huang, Y. L.; Chu, Y. Y.; Yan, D. C.; Wu, M. K. *Proc. Natl. Acad. Sci. U.S.A.* **2008**, *105*, 14262–14264.

(23) Farrell, D.; Majetich, S. A.; Wilcoxon, J. P. *J. Phys. Chem. B* **2003**, *107*, 11022–11030.

(24) Huber, D. L. *Small* **2005**, *1*, 482–501.

(25) Peng, S.; Wang, C.; Xie, J.; Sun, S. H. *J. Am. Chem. Soc.* **2006**, *128*, 10676–10677.

(26) Kim, D.; Park, J.; An, K.; Yang, N. K.; Park, J. G.; Hyeon, T. *J. Am. Chem. Soc.* **2007**, *129*, 5812–5813.

(27) Lacroix, L. M.; Lachaize, S.; Falqui, A.; Respaud, M.; Chaudret, B. *J. Am. Chem. Soc.* **2009**, *131*, 549–557.

(28) Sun, S. H.; Murray, C. B. *J. Appl. Phys.* **1999**, *85*, 4325–4330.

(29) Murray, C. B.; Sun, S. H.; Doyle, H.; Betley, T. *MRS Bull.* **2001**, *26*, 985–991.

(30) Puntes, V. F.; Krishnan, K. M.; Alivisatos, P. *Appl. Phys. Lett.* **2001**, *78*, 2187–2189.

(31) Sun, S. H.; Zeng, H. *J. Am. Chem. Soc.* **2002**, *124*, 8204–8205.

(32) Sun, S. H.; Zeng, H.; Robinson, D. B.; Raoux, S.; Rice, P. M.; Wang, S. X.; Li, G. X. *J. Am. Chem. Soc.* **2004**, *126*, 273–279.

(33) Zeng, H.; Rice, P. M.; Wang, S. X.; Sun, S. H. *J. Am. Chem. Soc.* **2004**, *126*, 11458–11459.

(34) Hyeon, T.; Lee, S. S.; Park, J.; Chung, Y.; Bin Na, H. *J. Am. Chem. Soc.* **2001**, *123*, 12798–12801.

(35) Hyeon, T. *Chem. Commun.* **2003**, 927–934.

(36) Park, J.; An, K. J.; Hwang, Y. S.; Park, J. G.; Noh, H. J.; Kim, J. Y.; Park, J. H.; Hwang, N. M.; Hyeon, T. *Nat. Mater.* **2004**, *3*, 891–895.

(37) Zeng, H.; Li, J.; Wang, Z. L.; Liu, J. P.; Sun, S. H. *Nano Lett.* **2004**, *4*, 187–190.

(38) Wang, C.; Hou, Y. L.; Kim, J. M.; Sun, S. H. *Angew. Chem., Int. Ed.* **2007**, *46*, 6333–6335.

(39) Kim, J. M.; Rong, C. B.; Liu, J. P.; Sun, S. H. *Adv. Mater.* **2009**, *21*, 906–909.

(40) Shevchenko, E. V.; Talapin, D. V.; Schnablegger, H.; Kornowski, A.; Festin, O.; Svedlindh, P.; Haase, M.; Weller, H. *J. Am. Chem. Soc.* **2003**, *125*, 9090–9101.

(41) Murray, C. B.; Norris, D. J.; Bawendi, M. G. *J. Am. Chem. Soc.* **1993**, *115*, 8706–8715.

(42) Alivisatos, A. P. *Science* **1996**, *271*, 933–937.

(43) Yin, Y. D.; Rioux, R. M.; Erdonmez, C. K.; Hughes, S.; Somorjai, G. A.; Alivisatos, A. P. *Science* **2004**, *304*, 711–714.

(44) Wang, Y. H. A.; Bao, N.; Shen, L.; Padhan, P.; Gupta, A. *J. Am. Chem. Soc.* **2007**, *129*, 12408–12409.

(45) Tang, J.; Hinds, S.; Kelley, S. O.; Sargent, E. H. *Chem. Mater.* **2008**, *20*, 6906–6910.

(46) Lin, C. R.; Yeh, C. L.; Lu, S. Z.; Lyubutin, I. S.; Wang, S. C.; Suzdalev, I. P. *Nanotechnology* **2010**, *21*, 235603.

(47) Oyler, K. D.; Ke, X. L.; Sines, I. T.; Schiffer, P.; Schaak, R. E. *Chem. Mater.* **2009**, *21*, 3655–3661.

(48) Chen, L. Q.; Zhan, H. Q.; Yang, X. F.; Sun, Z. Y.; Zhang, J.; Xu, D.; Liang, C. L.; Wu, M. M.; Fang, J. Y. *CrystEngComm* **2010**, *12*, 4386.

(49) Lin, C. R.; Siao, Y. J.; Lu, S. Z.; Gau, C. *IEEE Trans. Magn.* **2009**, *45*, 4275–4278.

(50) Shi, W. L.; Zeng, H.; Sahoo, Y.; Ohulchanskyy, T. Y.; Ding, Y.; Wang, Z. L.; Swihart, M.; Prasad, P. N. *Nano Lett.* **2006**, *6*, 875–881.

(51) Zeng, H.; Sun, S. H. *Adv. Funct. Mater.* **2008**, *18*, 391–400.